Journal of Applied Fluid Mechanics, Vol. 17, No. 4, pp. 756-769, 2024.
Available online at www.jafmonline.net, ISSN 1735-3572, EISSN 1735-3645.
https://doi.org/10.47176/jafm.17.4.2299

Large-eddy Simulations on Flow Structures and Interaction Mechanism of Synthetic Jets in a Crossflow

W. Quan, W. Sun†, J. Zhang and X. Tan

College of Energy and Power Engineering, Nanjing University of Aeronautics and Astronautics, Nanjing, 210016, China

†Corresponding Author Email: wjsun@nuaa.edu.cn

ABSTRACT

The results of large-eddy simulations are presented to illustrate the flow structures generated by the interaction of synthetic jets with a crossflow. The coupled calculations involving the internal flow of the actuator cavity and the external flow are performed using the ANSYS-Fluent software. The influence of the orifice shape (round orifice and rectangular orifices with aspect ratio of 6, 12, or 18) on the evolution of coherent structures is analyzed, and the effects of the jet-to-crossflow velocity ratio (0.5, 1.0, or 1.5) on the turbulent flow behavior are examined. The results show that the first vortex ring shed from the rectangular orifice lip behaves as a plate-like vortex. The horseshoe vortex and first vortex ring are followed by a trailing jet in the case of a round orifice, but this configuration is rarely identified when the orifice is rectangular. For the rectangular orifice with an aspect ratio of 18, the plate-like vortex splits into vortex filaments that become interwoven with the center of the synthetic jet. In general, at the same characteristic velocity, the round-orifice synthetic jet has a stronger capacity for normal penetration into the crossflow, whereas the rectangular-orifice synthetic jet with a large aspect ratio develops closer to the wall. For the rectangular orifice with a large aspect ratio, the development of the synthetic jet is restricted to a small region near the wall at a small jet-to-crossflow velocity ratio.

Article History

Received September 7, 2023
Revised November 3, 2023
Accepted November 17, 2023
Available online January 30, 2024

Keywords:

Synthetic jet
Jet-in-crossflow
Interaction flow structure
Orifice shape
Large-eddy simulation

1. INTRODUCTION

A synthetic jet is a special flow phenomenon generated using functional actuators, which stimulate the surrounding fluid to form a self-synthesized flow (Glezer & Amitay, 2002; Zhou et al., 2022). As synthetic jets have a unique zero-net-mass-flux property, they provide a novel active flow control scheme that has been employed in practical applications such as flow separation suppression, thrust vector control, mixing augmentation, and heat transfer enhancement (Li et al., 2016; Arshad et al., 2020; Li et al., 2022).

In the fields of flow control and heat transfer enhancement, the mutual interaction mechanism between a jet and a crossflow (jet-in-crossflow) is a fundamental problem (Mahesh, 2013). Typical applications associated with the jet-in-crossflow configuration include aerodynamic vector control based on jet injection, the temperature field regulation of a combustion chamber based on jet mixing, and jet impingement heat transfer with an initial crossflow. In general, the mutual interaction mechanism within a jet-in-crossflow is very complicated. The coherence of the crossflow and the jet generates a series of complex vortex structures, including shear layer vortices, counter-rotating vortex pairs, horseshoe vortices, and wake vortices. The jet injection produces a boundary-layer disturbance that affects the local crossflow, and the crossflow directly impacts the trajectory development of the jet. In recent decades, the coherent mechanism of conventional continuous jets in a crossflow has been extensively studied (Karagozian, 2014; Feng et al., 2018; Turkyilmazoglu, 2019; Zhang et al., 2020; Jafarimoghaddam et al., 2021). The mutual interaction between the jet and the crossflow is known to induce complex vortex structures. To enable flow control in the case of jet-in-crossflow problems, many active and passive strategies have been developed based on fluidic, pulsed, and acoustic excitations (Eroglu & Breidenthal, 2001; Zaman & Milanovic, 2012; Shoji et al., 2019; Ostermann et al., 2020; Quan et al., 2023).

NOMENCLATURE

ν_t	a vorticity viscosity coefficient	ν	the viscosity coefficient of the fluid
D_c	the cavity diameter of synthetic jet actuator	A	the diaphragm amplitude
h_c	the cavity hight of synthetic jet actuator	f	excitation frequency
h_n	neck height of the orifice	t	time
h_0	width of the orifice	T	time period of the cycle
l_0	length of the orifice	U_∞	the velocity of the crossflow
D	diameter of round orifice	U_0	the characteristic velocity of the synthetic jet
C_b	velocity ratio of cross flow to the synthetic jet	δ^*	the displacement thickness
φ	phase angle of the motion period	θ	the momentum thickness
u	instantaneous velocity vector	H	the boundary layer shape ratio
ω_z	vorticity in the z-direction	Δ	filter feature width
ω_x	vorticity in the x-direction	ρ	the density of the fluid
Re_θ	Reynolds number based on momentum boundary layer thickness	AR	aspect ratios which defined as length l_0 to width h_0 of the orifice
δ	the boundary layer thickness		

Compared with continuous jets, synthetic jets have a highly vortex-dynamics-driven nature that is induced by a series of coherent vortex rings. Hence, they possess a stronger shearing ability, which disturbs the surrounding fluid at a variety of length scales and produces more sophisticated flow behaviors (Smith & Swift, 2003; Tan et al., 2015; Xia & Mohseni, 2018; Rathay & Amitay, 2022). To date, many studies have focused on the development and evolution of synthetic jets in a quiescent environment. However, in a crossflow, the difference between the external flow environments makes the evolution of synthetic jets quite different from that in the quiescent environment, both in the near field and the far field (Wu & Leschziner, 2009).

Existing studies on the mutual interaction behaviors of synthetic jets can be broadly divided into two categories. First, several researchers have focused on the active control of the boundary layer of the main flow, including the formation and evolution of the unsteady vortex structures induced by the synthetic jets and the time-averaged flow characteristics in the near-wall region (Jabbal & Zhong, 2008; Wen & Tang, 2014; Berk et al., 2018; Jankee & Subramani, 2021). In this situation, the synthetic jets generally have a relatively weak injection intensity and smaller penetration capacity. Second, viewed in terms of mixing and heat transfer enhancement, research has mainly concerned the development and evolution of synthetic jets in the far-field region and the mixing and heat transfer processes (Eri et al., 2016; Gordon & Soria, 2002; Xia & Mohseni, 2017). In this case, the synthetic jets generally have a relatively strong injection intensity and larger penetration capacity. Previous research has identified that the mutual interaction between the synthetic jets and the crossflow induces a series of vortical structures with different scales. In comparison with continuous jets (Zhang et al., 2013), synthetic jets have a substantially more complex influence mechanism because of their unstable evolution and flow schemes. In particular, the orifice shape has a significant effect on the spatiotemporal evolution of synthetic jets. For instance, Garcillan et al. (2004) performed particle image velocimetry measurements on the synthetic jets ejected from rectangular orifices with different aspect ratios and round orifices with different inclination angles. Their results showed that higher aspect ratios or inclination angles produce jets with higher initial momentum and vorticity. However, in the far field, the greater necessity for the distorted vortex rings to rearrange themselves into more stable structures means that the intensity of the synthetic jets tends to decrease rapidly. A series of studies (Elimelech et al., 2011; Sahni et al., 2011; Van Buren, et al., 2014, 2016a, 2016b) have investigated the coherence process of finite-span synthetic jets with different aspect ratios in a crossflow. These have identified that the shape of the synthetic-jet orifice has a more important influence on the coherent flow structures than the orifice neck depth. Increasing the orifice aspect ratio gradually reduces the size of the edge vortex and makes the secondary flow structure in the near field more obvious. Reducing the orifice aspect ratio weakens the aerodynamic blockage effect near the orifice outlet, making the downstream vortex structures more stable in the far field.

The complex coherent behavior of synthetic jets in a crossflow is tightly related to the orifice shape and the velocity ratio. Despite numerous studies, the complex vortical structures and their spatiotemporal evolution mechanism require further identification. In the present study, the large-eddy simulation (LES) methodology is adopted to illustrate the coherent flow structures of synthetic jets in a crossflow, wherein the influence of the aspect ratio for a rectangular orifice and the jet-to-crossflow velocity ratio are of primary concern. From direct comparisons between several rectangular orifices and a round orifice with the same orifice area, the coherent flow characteristics are illustrated in detail, providing an in-depth understanding of the mutual interaction mechanism of synthetic jets in a crossflow.

2. COMPUTATIONAL MODEL

The synthetic jet actuator model used in the present study follows the experimental model of a finite-span rectangular-orifice synthetic jet studied by Van Buren et al. (2016a), as schematically shown in Fig. 1(a). Figure 1(b) displays a schematic diagram of the computational model, where the synthetic jet actuator is located beneath the wall of a crossflow or external flow. The size of the crossflow is L_x/D = 32 (streamwise length in x-direction), L_y/D = 10 (spanwise width in y-direction), and L_z/D = 10 (normal height in z-direction). The synthetic jet actuator cavity is cylindrical, as shown in Fig. 1(c). According to Van Buren et al. (2016a), the cavity diameter and cavity height are D_c = 39.7 mm and h_c = 1 mm, respectively. The neck height of the orifice is h_n = 6 mm. In the present study, a round orifice and three rectangular orifices with different aspect ratios (*AR*, defined as length l_0 divided by height h_0 of the orifice) are designed, as shown in Fig. 1(d). All orifices have the same outlet area or the same equivalent diameter as the round orifice, D = 4.79 mm. The three *AR*s of the rectangular orifices are 6, 12, and 18. Corresponding to *AR* = 18, the length and width are l_0 = 18 mm and h_0 = 1 mm, respectively. The origin of the coordinate system is the center of the cross-section of the synthetic jet outlet.

The boundary conditions of the calculation model are also shown in Fig. 1(b). The crossflow inlet is assigned a velocity inlet condition, and the outlet is taken as the zero-pressure outlet. The other walls (except the symmetric wall) are assumed to be no-slip walls. In the present study, the crossflow velocity is maintained at U_∞ = 10 m/s. In accordance with a low-Reynolds-number boundary-layer experiment (Purtell & Klebanoff, 1981) and the research of Ho et al. (2022), the mean velocity profile is assigned at the inlet boundary with 0.5% flow direction turbulence intensity. Figure 2 shows the velocity profile at the x/D = −2 section upstream of the orifice alongside the experimental data of Purtell and Klebanoff (1981). The figure demonstrates that the simulation and experiment results concur to a satisfactory degree. The Reynolds number based on the momentum boundary-layer thickness is Re_θ = 950, the boundary layer thickness is δ = 14 mm, the displacement thickness is δ^* = 2.1 mm, the momentum thickness is θ = 1.42 mm, and the boundary layer shape ratio is H = 1.48. The crossflow temperature is 300 K and the ambient pressure is 101325 Pa. For the synthetic jet, the motion of the bottom diaphragm of the synthetic jet actuator is assumed to be planar and to vary sinusoidally with time according to Eq. (1). The excitation frequency is fixed at f = 1125 Hz. By adjusting the vibration amplitude A, the periodic expulsion and ingestion status of the synthetic jet can be changed, thus modifying the characteristic velocity U_0 of the synthetic jet and the velocity ratio C_b.

$$y(r,t) = A\sin(2\pi ft) \tag{1}$$

$$U_0 = \frac{1}{T}\int_0^{T/2} u_j(t)dt \tag{2}$$

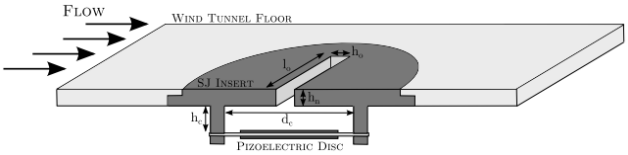

(a) Synthetic jet actuator model (Van Buren, et al., 2016a)

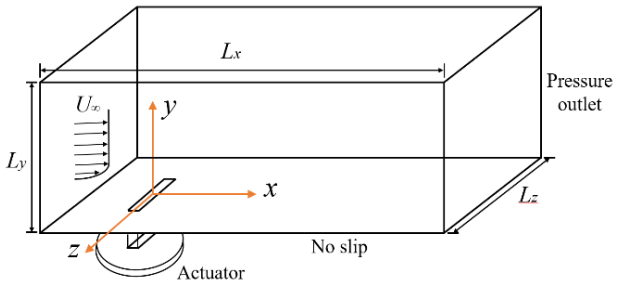

(b) Computational model

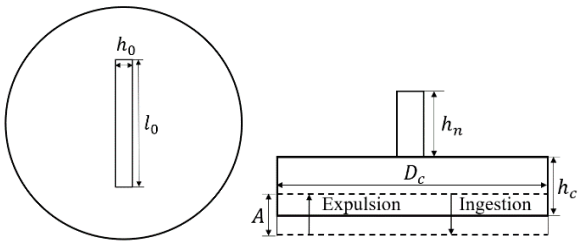

(c) Actuator structure parameters

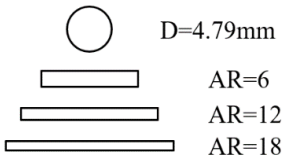

(d) Orifice shape

Fig. 1 Schematic physical and computational models

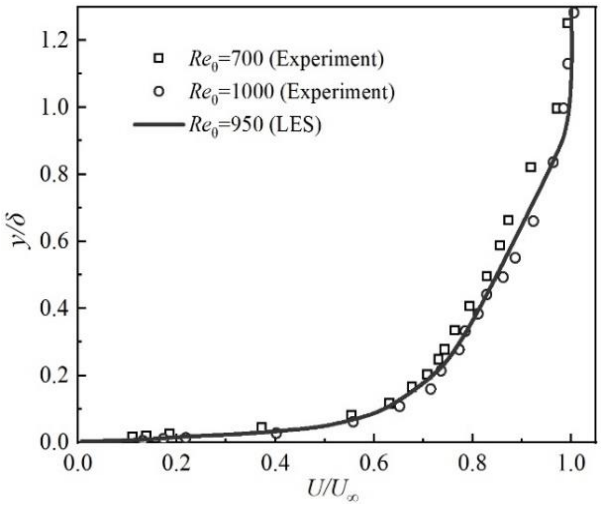

Fig. 2 Velocity profile at x/D = −2 upstream of the orifice and experimental results (Purtell & Klebanoff, 1981)

$$C_b = \frac{U_0}{U_\infty} \tag{3}$$

here f is the excitation frequency, A is the diaphragm amplitude, t is time, T is the time period of one cycle, and $u_j(t)$ is the instantaneous velocity of the synthetic jet at the orifice. In this study considers velocity ratios of 0.5, 1.0, and 1.5.

3. COMPUTATIONAL METHODOLOGY

3.1 Large-Eddy Simulations

The LES method is used for the numerical calculations. In the LES framework, the flow variable $f(x,t)$ can be decomposed into a large-scale component $\tilde{f}(x,t)$ and a small-scale component $f'(x,t)$, that is,

$$f(x,t) = \tilde{f}(x,t) + f'(x,t) \tag{4}$$

The large-scale component $\tilde{f}(x,t)$ is highly dependent on time, as realized using a filtering function G:

$$\tilde{f}(x,t) = \iiint G(x,x')f(x',t)dx^3x' \tag{5}$$

The present study uses a box filter defined as

$$G(x,x') = \begin{cases} \frac{1}{\Delta} \forall |x,x'| \le \frac{1}{2}\Delta \\ 0 \forall |x,x'| > \frac{1}{2}\Delta \end{cases} \tag{6}$$

where Δ is the filter feature width.

The key to the LES method is to identify the correct subgrid model. In this study, Smagorinsky's model based on the vortex viscosity hypothesis is adopted:

$$\tau_{ij} - \frac{\sigma_{ij}}{3}\tau_{kk} = -2\nu_t \bar{S}_{ij} = -2C_S^2\Delta^2 |\bar{S}| \bar{S}_{ij} \tag{7}$$

where δ_{ij} is Kronecker's delta function, ν_t is the vorticity viscosity coefficient, and C_s is the Smagorinsky constant. The large-scale strain rate tensor is

$$\bar{S}_{ij} = \frac{1}{2}\left(\frac{\partial \bar{u}_i}{\partial x_j} + \frac{\partial \bar{u}_j}{\partial x_i}\right) \tag{8}$$

In the LES framework, filtering functions are applied to the flow field to distinguish between vortices of different scales. After filtering, the large-scale vortex part is solved by direct calculation, whereas the small-scale vortex part is solved by modeling. Following box filtering, the control equation is expressed as follows (Grenson & Deniau, 2017):

$$\frac{\partial \rho \tilde{u}_i}{\partial x_i} = 0 \tag{9}$$

$$\frac{\partial \tilde{u}_i}{\partial t} + \frac{\partial \tilde{u}_i \tilde{u}_j}{\partial x_j} = -\frac{1}{\rho}\frac{\partial \bar{p}}{\partial x_i} + \nu \frac{\partial}{\partial x_j}\left[\frac{\partial \tilde{u}_i}{\partial x_j} + \frac{\partial \tilde{u}_j}{\partial x_i}\right] - \frac{1}{\rho}\frac{\partial \tau_{ij}^S}{\partial x_j} \tag{10}$$

where ρ is the density of the fluid, v is the viscosity coefficient of the fluid, and τ_{ij}^S is the sublattice-scale stress term, expressed as follows:

$$\tau_{ij}^S = \rho\left(u_i u_j - \tilde{u}_i \tilde{u}_j\right) \tag{11}$$

3.2 Computational Process

The coupled calculations concerning the internal flow inside the actuator cavity and the external flow are performed using the ANSYS-Fluent software. The motion of the vibrating diaphragm is solved using a dynamic mesh and user-defined functions. The dynamic mesh is varied by layering. A structured grid is applied to the entire fluid domain, and a boundary-layer grid is applied in the near-wall region. An example of the computational grid system for the rectangular-orifice synthetic jet with a high *AR* is shown in Fig. 3. In this study, the number of grid cells is approximately 20 million, wherein the size of the first layer grid is 0.001 mm and the grid growth rate in the normal direction is 1.1. The neighboring-cell y^+ value of this computational grid system is less than 1. A grid independence test shows that the computational results are affected by the control volume. For the round-orifice model with a velocity ratio of 1.0, grid independence was investigated by modifying the number of cells from 6.7 million to 20.5 million. The average velocity of the synthetic jet exit was used as the key parameter for comparing the various mesh sizes. The results show that the deviation of the average exit velocity from the theoretical value decreases from 7.8% to 2.83% as the number of cells increases from 6.7 million to 13.2 million. The deviation is 1.5% with 20.5 million cells. In this paper, the streamwise velocity at the point (-3D, 6D, 0) is monitored and the power spectral density curve of the velocity is plotted. From Fig. 4, in the inertial sub region of turbulence, the slope of the power spectral density conforms to -5/3, which proves the reliability of grid resolution.

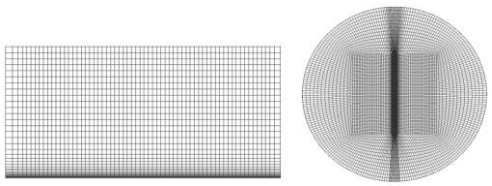

(a) Crossflow zone (b) Actuator cavity

Fig. 3 Local grids

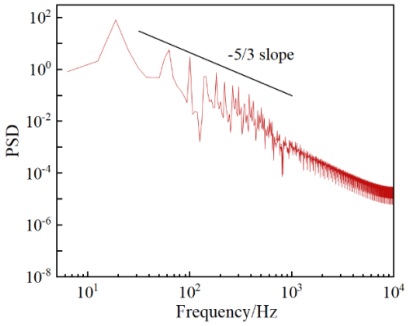

Fig. 4 Power spectral density based on *x*-direction velocity on the z/D=0 plane

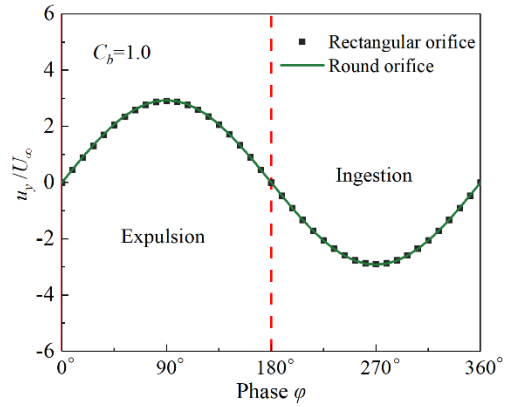

(a) Round and rectangular orifices (*AR* = 18)

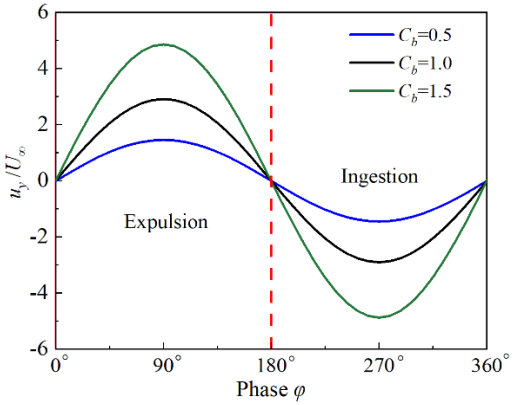

(b) Different C_b

Fig. 5 Instantaneous velocity variation at orifice outlet

Figure 5 shows the instantaneous velocity variation at the synthetic-jet orifice outlet during one period. In this figure, the crossflow velocity is used as a reference for the dimensionless velocity; u_y is the velocity component of the synthetic jet in the *y*-direction and φ is the phase angle. When φ is in the range 0°–180°, the synthetic jet operates in the expulsion phase, whereas from 180°–360°, the jet is in the ingestion phase. The instantaneous velocity changes sinusoidally, agreeing with the actuator diaphragm movement. Figure 5(a) shows that the orifice shape has almost no effect on the instantaneous velocity of the synthetic jet at the orifice outlet. This is because all orifice shapes in the present study have the same exit area. Therefore, in the case of a low-speed incompressible flow, the orifice shape does not influence the characteristic velocity U_0 of the synthetic jet for a fixed volume of air ejected from the actuator orifice during the ejection portion of the cycle. Figure 5(b) indicates that the crossflow has almost no effect on the sinusoidal distribution of the instantaneous velocity for the various synthetic jet orifices.

The subgrid used in this study is the Smagorinsky–Lilly model. The pressure–velocity coupling adopts the SIMPLE algorithm. An unsteady implicit solver is used for the numerical simulations, with a second-order implicit scheme used for transient terms and a least-squares cell-based scheme applied for gradient terms. Convergence is reached when the residual of each solution is less than 1×10^{-5}. The time step is 2.22×10^{-5} s and 50 sub-iterations are implemented in an inner loop during each time step. The calculations are performed on a supercomputer with an Intel(R) Xeon(R) CPU E5-2683. Forty-five cycles of computation require 60000 cores in total.

3.3 Computational Method Verification

To validate the current numerical procedure, a validation example is compared with the experimental finite-span rectangular orifice model (*AR* = 18) of Van Buren et al. (2016a). Figures 6 and 7 present the instantaneous coherence structures obtained at four phases under C_b = 1.5 from the particle image velocimetry tests

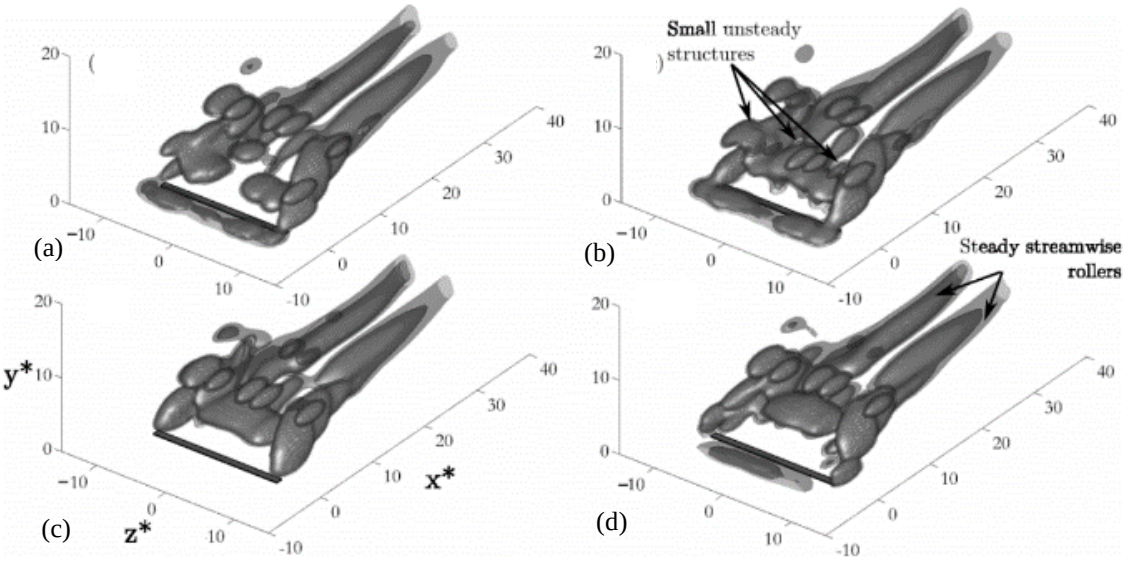

Fig. 6 Instantaneous vortical structures identified by *Q*-criterion at four phases taken from (Van Buren et al., 2016a). (a) φ = 0°, (b) φ = 90°, (c) φ = 180°, (d) φ = 270°

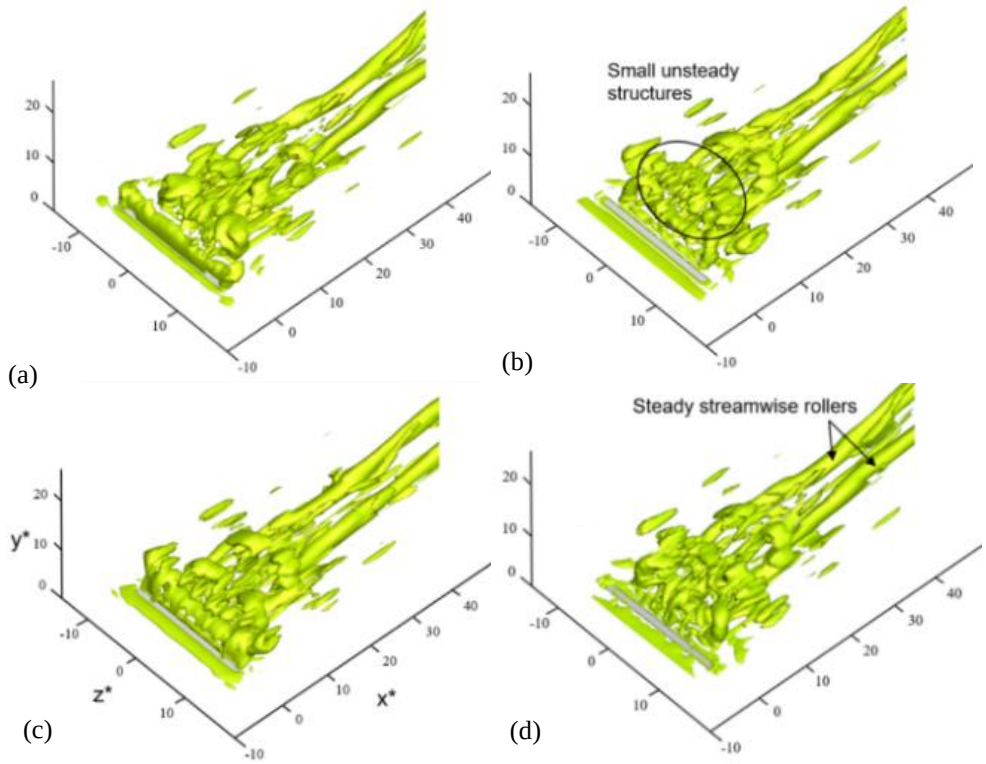

Fig. 7 Instantaneous vortical structures identified by *Q*-criterion at four phases using the present LES (a) φ = 0°, (b) φ = 90°, (c) φ = 180°, (d) φ = 270°

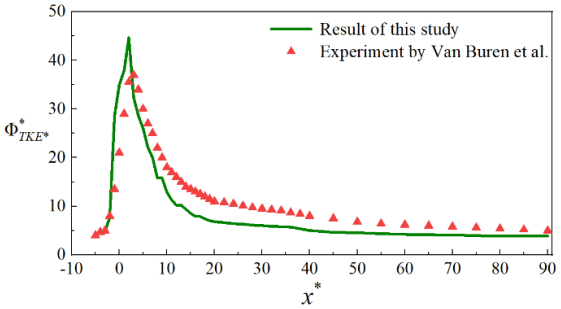

Fig. 8 Streamwise evolution of the integrated TKE at C_b = 1.5

of Van Buren et al. and the current LES simulations, respectively. These structures are identified according to the *Q*-criterion (*Q*=0.2) (Hunt et al., 1988). The present LES simulations are highly consistent with the experimental results. In general, the flow field can be divided into the near field, where the flow is unsteady, and the far field, where the flow is quasi-steady. Immediately downstream of the orifice, the large-scale vortices induced by shearing at the orifice outlet break into small-scale vortices. These small-scale vortices gradually develop downstream to form quasi-steady streamwise rollers, undergoing complicated dissipation, shrinkage, and aggregation. Upon the impact of the crossflow, the vortical structures are deflected toward the wall. The vortices at both spanwise sides dissipate, and those at the center aggregate to form concentrated strip-shaped vortical structures, which penetrate into the crossflow. Figure 8 shows the area-integrated turbulent kinetic energy (TKE) on the sectional plane along the streamwise direction. The TKE reaches a peak value immediately downstream of the orifice and then decays gradually along the streamwise direction. From this quantitative comparison, it is clear that the present numerical methodology is satisfactory.

4. RESULTS AND DISCUSSION

4.1 Effects of Orifice Shape

This section presents a comparative analysis of the different orifice shapes. We focus on illustrating the effects of the orifice shape on the evolution of the vortical coherent structures.

First, we compare the round orifice with the rectangular orifice (*AR* = 18) in a quiescent environment (U_∞ = 0). Figure 8 shows the three-dimensional vortical structures of the synthetic jet, identified by the *Q*-criterion (*Q*=2). During the expulsion stage (φ in the range 0°–180°), the fluid inside the actuator cavity is ejected from the orifice, wherein a shear-induced vortex ring forms at the orifice outlet. In the ingestion stage (φ in the range 180°–360°), the surrounding fluid is sucked into the cavity, while the initial vortex ring develops downstream under its own momentum. After a certain number of cycles, the flow pattern of the synthetic jet exhibits periodic stability. Although the vortical structures experience continuous changes in different phases, the primary vortex ring has almost the same structural features, generally reflecting the orifice shape.

Figure 10 shows the three-dimensional vortical structures in a crossflow of C_b = 1.5, as identified by the *Q*-criterion (*Q*=2). The initial structure generated by orifice shearing that is shed from the orifice lip is termed

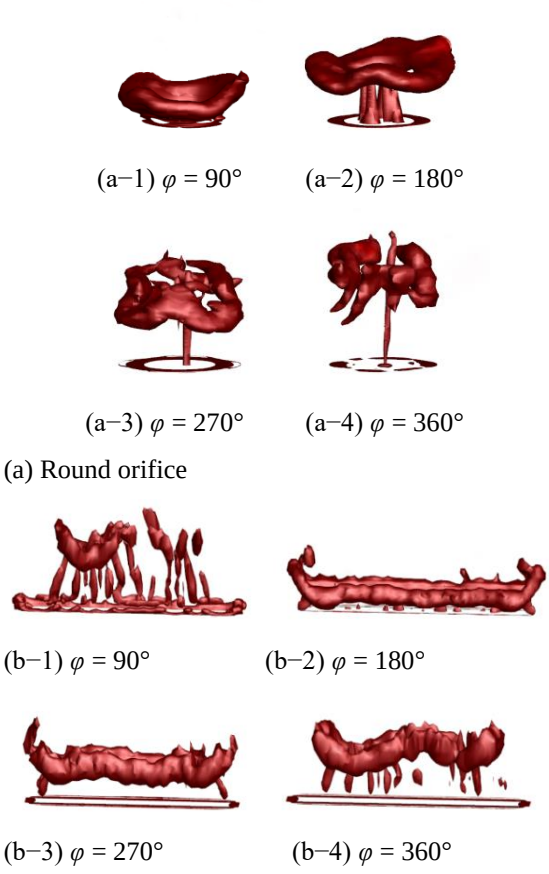

Fig. 9 Instantaneous vortical structures identified by *Q*-criterion in a quiescent environment

the first vortex ring (FVR). When compared with the quiescent environment, the coherent vortical structures induced by the mutual interaction between the synthetic jet and the crossflow are more complicated and are strongly affected by the orifice shape.

In the case of the round orifice, Fig. 10(a) shows that the FVR is concentrated in the space surrounding the orifice. When the forced external flow passes across it, a horseshoe vortex (HV) structure is induced during the expulsion stage, originating from the front side of the FVR. The HV wraps around the FVR and moves downstream. At the same time, the shearing of the crossflow and the jet creates a hanging vortex pair that tilts in the streamwise direction upon the impact of the crossflow. Finally, this evolves into a counter-rotating vortex pair (CVP), which is an inherent feature of jet-in-crossflow dynamics. In the ingestion stage, the near field downstream of the orifice is mainly dominated by the HV and CVP, both of which continue to develop downstream under the effects of the synthetic jet. During this stage, the initial FVR clearly remains at the front of the trailing jet, experiencing deformations in each stage and persisting into the next cycle.

For the rectangular orifices, the FVR develops into a plate-like vortex (PV) immediately downstream of the orifice outlet during the expulsion stage. When compared with the round orifice, the FVR has a longer spanwise extent, but a narrower streamwise width. Because of the structural feature of the FVR, the windward side of the synthetic jet suffers an obvious impact from the crossflow, generating wavy or even cut PV isosurfaces. Additionally, as the PV is narrow in the streamwise direction, it is difficult for HVs to be induced in the crossflow.

Compared with the round orifice, the FVR of the rectangular orifice is easily destroyed by the crossflow. Therefore, the initial FVR rarely remains at the front of the trailing jet. Figure 10 confirms that the *AR* of the rectangular orifice has a significant effect on the evolution of coherent vortical structures. When *AR* = 6, as shown in Fig. 10(b), the middle part of the PV splits as the expulsion stage becomes the ingestion stage (φ = 180°). Two relatively isolated jets are then formed within a specific time interval, such that two CVPs appear at φ = 270°. At φ = 360°, the leading CVP develops and the trailing CVP gradually diminishes, so that only one CVP remains in the next cycle. For *AR* = 12, as shown in Fig. 10(c), the PV breaks into multiple vortex strings at the end of the expulsion stage. For the rectangular orifice with *AR* = 18, vortex-filament (VF) structures obviously occur at φ = 180°, as shown in Fig. 10(d). As the VFs have a small scale, they intertwine downstream, so that no independent CVPs are generated. Indeed, CVPs are only generated at the edges of the flow domain. The vortical structures are deflected toward the wall more strongly in the case of rectangular.

Orifices with larger *AR*s. As *AR* increases, the FVR becomes more unstable because synthetic jets with narrower orifices are more strongly influenced by the crossflow, making the FVR more susceptible to destruction.

Figure 11 shows the instantaneous velocity vector and the dimensionless streamwise velocity distribution (u/U_∞) on the centerline plane (z/D = 0). The mutual interaction between the synthetic jet and the crossflow has several identical or similar features, regardless of the orifice shape.

First, during the expulsion stage of the synthetic jet, the replenishment of momentum by the shear vortex ring at the orifice allows the synthetic jet to produce a strong blocking role on the crossflow, resulting in a localized recirculation flow upstream of the orifice. This blocking role is more obvious for the round orifice because the associated synthetic jet is more concentrated. During the ingestion stage, the inhalation of surrounding fluid into the actuator cavity imposes a suction effect on the boundary-layer flow, and so a local acceleration effect occurs in the near-wall zone upstream of the orifice. Second, downstream of the orifice, the synthetic jet lifts away from the wall, and wake flow and recirculating flow zones form beneath the jet. The shearing of the synthetic jet and the crossflow induces a complicated interaction. The supplementary momentum supplied by the synthetic jet into the crossflow causes localized flow acceleration of the crossflow due to the shearing and mixing between them.

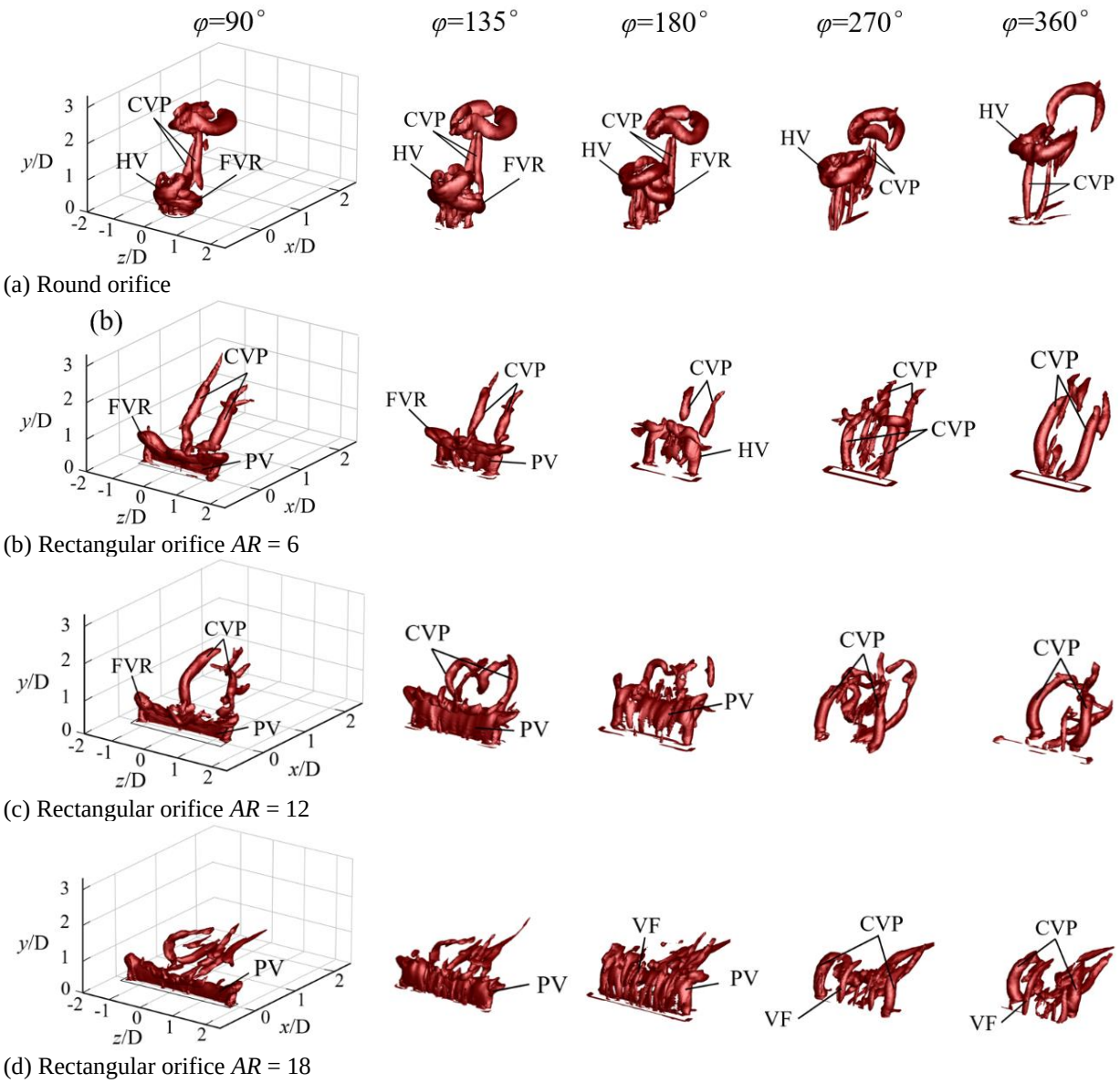

Fig. 10 Instantaneous vortical structures identified by *Q*-criterion in a crossflow

Additionally, the impact of the crossflow deflects the synthetic jet towards the wall. In general, the round-orifice synthetic has a stronger capacity to penetrate the crossflow than the rectangular orifices at the same characteristic velocity. As shown in Fig. 11(a), the FVR strongly influences the shearing in the flow field. Figure 11(d) indicates that the synthetic jet issuing from the rectangular orifice with a large *AR* develops closer to the wall.

Figure 12 depicts the dimensionless streamwise vorticity distribution ($\omega_x D/U_\infty$) on the streamwise sections. Although the synthetic jet is created by the aggregation of a succession of vortex rings generated by periodic shearing at the orifice outlet, it nevertheless exhibits inherent jet-in-crossflow dynamic characteristic of a downstream flow field dominated by a CVP. However, the evolution of the vortical structures in the near-field region of the orifice is more complex because of the strong pulsation characteristics of the synthetic jet. For the round orifice, the FVRs of the synthetic jet play more obvious roles in the crossflow. For the rectangular orifices, the PV separates into several small-scale vortex strings in the crossflow, and the scale of the CVP is significantly smaller than for the round orifice. For instance, in the region immediately downstream of the orifice (i.e., x/D = 1 and 5) many small-scale vortices develop, especially for the rectangular orifice with a high *AR*. These vortices progressively entwine and agglomerate to produce a rather large-scale CVP in the far field (i.e., x/D = 10 and 15). This may be attributed to the flow characteristics of the synthetic jet, namely its unstable near-field flow and relatively steady far-field flow. Moreover, it is also clear that the core of the CVP is lifted far from the wall in the case of the round orifice, indicating that the round-orifice synthetic jet has a stronger capacity to penetrate into the crossflow. In contrast, the rectangular-orifice synthetic jet with a large *AR* has a stronger flow capacity close to the wall. Figure 13 depicts the time-averaged jet center trajectory on the central plane,

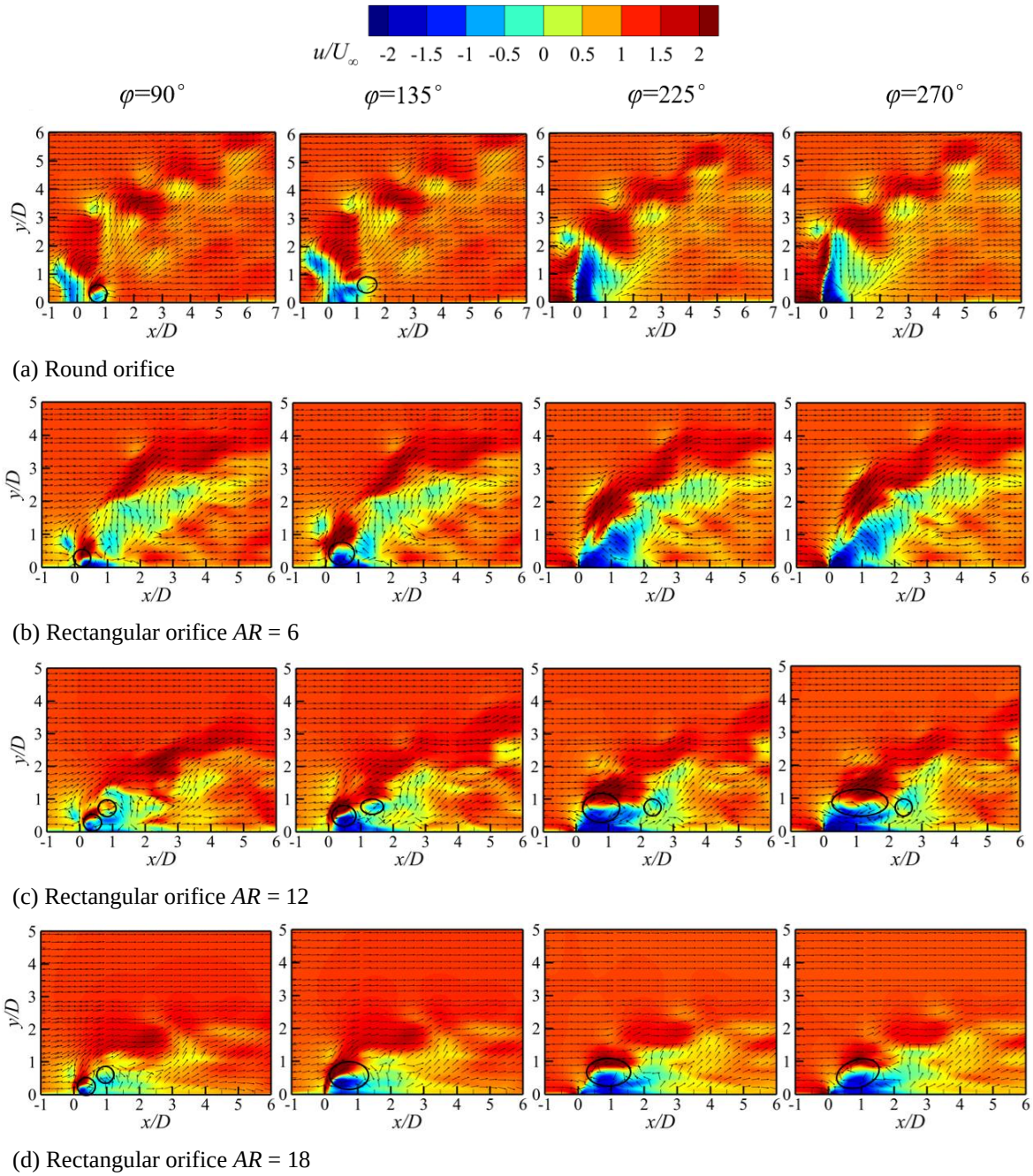

(a) Round orifice

(b) Rectangular orifice *AR* = 6

(c) Rectangular orifice *AR* = 12

(d) Rectangular orifice *AR* = 18

Fig. 11 Dimensionless streamwise velocity distribution on the central plane (*z*/*D* = 0)

based on the periodic time-homogenization treatment. This figure directly and intuitively demonstrates the penetration depths of the synthetic jets corresponding to different orifice shapes.

The time-averaged TKE distributions on the central plane are shown in Fig. 14. The high-turbulence effect of synthetic jet excitation mainly occurs within 8*D* of the orifice. As the synthetic jet issuing from the round orifice has a greater normal penetration capacity, it possesses a stronger ability to disturb and mix the crossflow in the normal direction, but a lesser ability in the streamwise direction. However, the synthetic jet from the rectangular orifice with a large *AR* has a stronger flow capacity close to the wall, and so the disturbance on the near-wall flow is significantly enhanced. Additionally, the pulsation of small-scale vortex clusters contributes to the turbulence enhancement in the near-wall flow. Figure 15 displays the area-integrated TKE distributions along the streamwise direction. The peak area-integrated TKE appears immediately downstream of the orifice. This is caused by the strong shearing disturbance of the near-field vortex rings induced by the synthetic jet. The peak area-integrated TKE is greater in the round-orifice case than for the *AR* = 18 rectangular-orifice case. Thisis because of the strong normal penetration generated by the round orifice and the disturbance of the vortex cluster near the wall with the rectangular orifice. The rectangular-orifice synthetic jet with a large *AR* has a strong ability to extend downstream, and so the area-integrated TKE

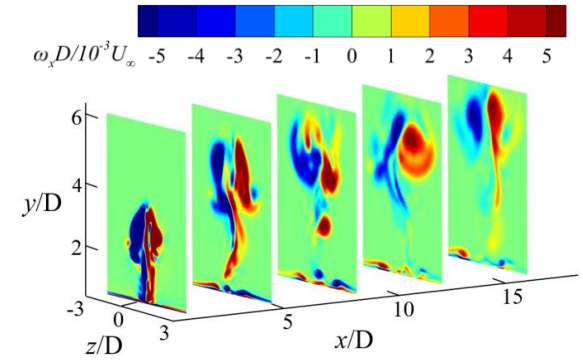

(a) Round orifice

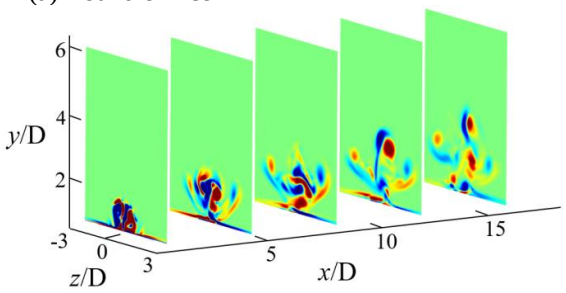

(b) Rectangular orifice *AR* = 6

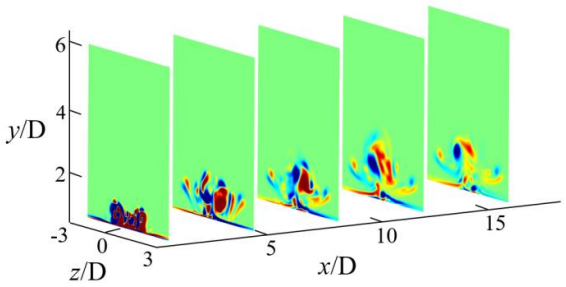

(c) Rectangular orifice *AR* = 12

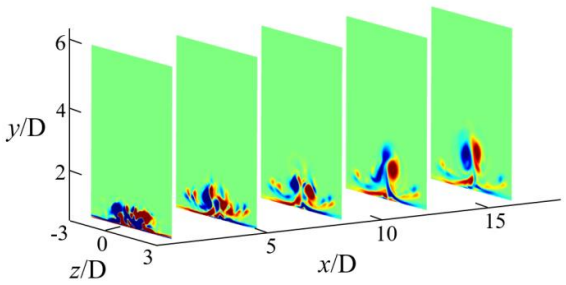

(d) Rectangular orifice *AR* = 18

Fig. 12 Dimensionless streamwise vorticity distribution on streamwise sections

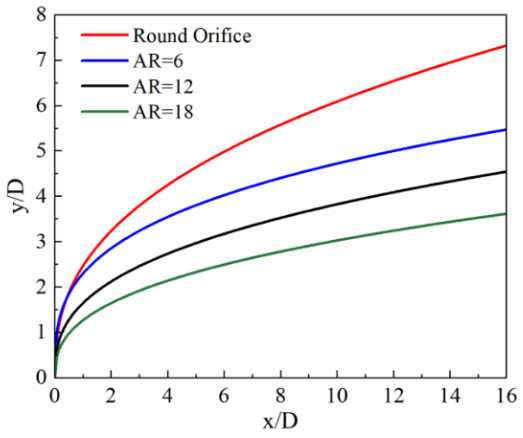

Fig. 13 Jet center trajectory on the central plane

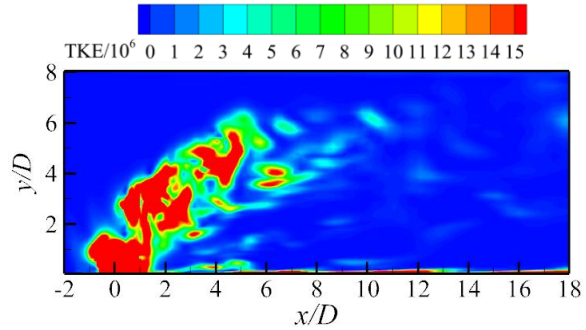

(a) Round orifice

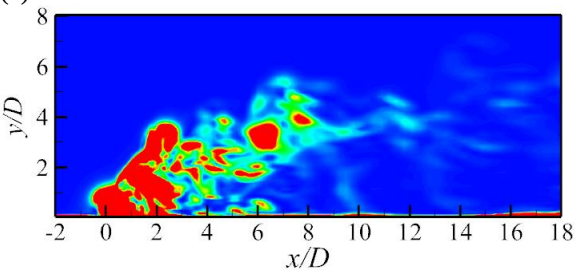

(b) Rectangular orifice *AR* = 6

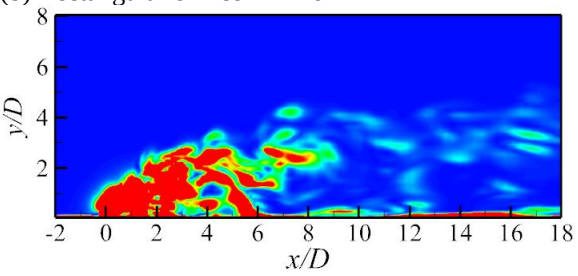

(c) Rectangular orifice *AR* = 12

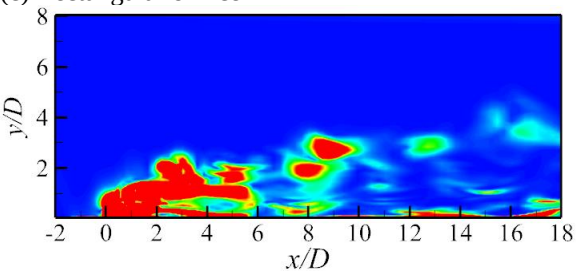

(d) Rectangular orifice *AR* = 18

Fig. 14 TKE distribution on the central plane (z/D = 0)

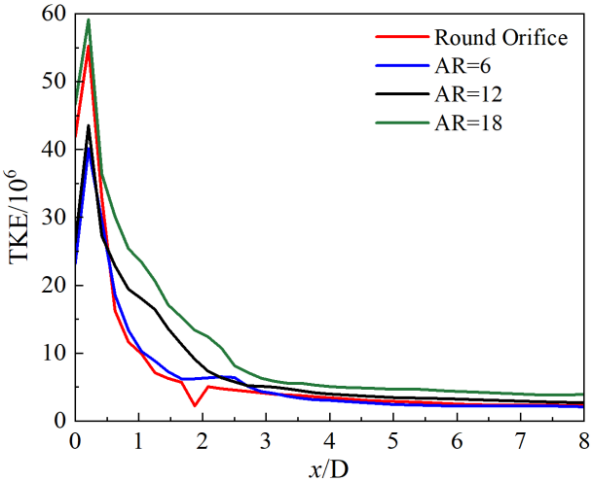

Fig. 15 Streamwise evolution of the area-integrated TKE

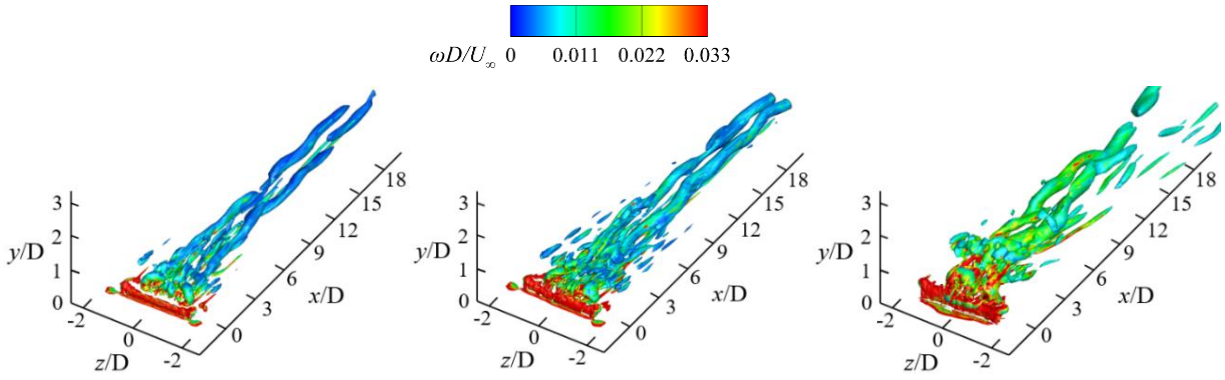

(a) C_b = 0.5 (b) C_b = 1.0 (c) C_b = 1.5

Fig. 16 Instantaneous vortical structures identified by *Q*-criterion for *AR* = 18 rectangular orifice

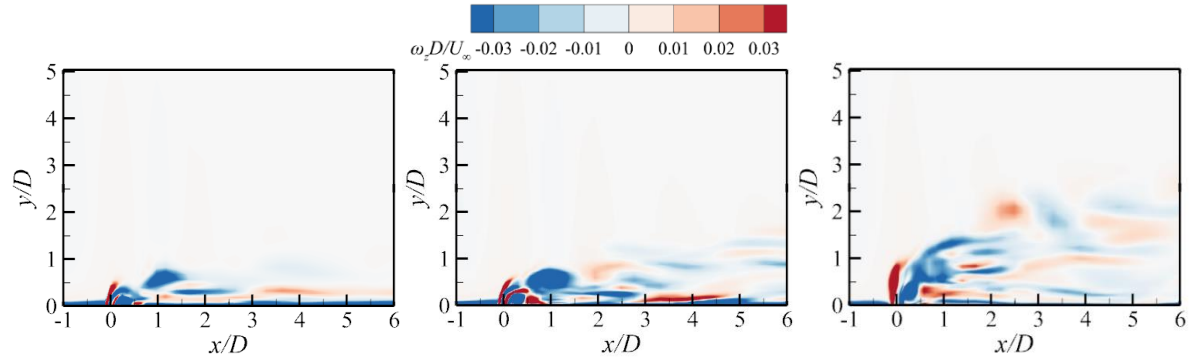

(a) C_b = 0.5 (b) C_b = 1.0 (c) C_b = 1.5

Fig. 17 Dimensionless vorticity distribution ($\omega_z D/U_\infty$) on the central plane

decays slowly along the streamwise direction. Therefore, the round-orifice synthetic jet is more suitable for use in mixing enhancement, and the rectangular-orifice synthetic jet with a large *AR* is more suitable for boundary-layer flow control applications.

4.2 Effects of Velocity Ratio

This section focuses on the rectangular orifice with *AR* = 18. We analyze the effects of the velocity ratio on the mutual interaction between the synthetic jet and the crossflow.

Figure 16 shows the vortical structures colored by the dimensionless vorticity, as identified by the *Q*-criterion. In a constant-velocity crossflow, increasing the jet-to-crossflow velocity ratio is equivalent to the synthetic jet having a higher injection velocity or momentum. Therefore, both the normal penetration and the zone of influence of the synthetic jet in the crossflow are enhanced. At a small velocity ratio, Fig. 16(a) shows that the size of the edge vortex obviously shrinks, indicating that a synthetic jet with weaker injection momentum is easily affected by the crossflow. At a large velocity ratio, Fig. 16(c) shows that the shearing role of the synthetic jet on the crossflow is significantly enhanced, producing higher vorticity in the far field. Regardless of the velocity ratio, a high-vorticity zone appears immediately downstream of the orifice. Increasing the characteristic velocity of the synthetic jet enhances the scale of the PV at the orifice outlet. Figure 16 suggests that the region $x/D \in [0, 3]$ is occupied by small-scale vortices, contributing to the unstable flow in the near field. In the far-field region $x/D \in [6, 18]$, two relatively stable streamwise vortices are dominant.

Figure 17 shows the dimensionless vorticity distribution ($\omega_z D/U_\infty$) on the central plane. For a small velocity ratio, Fig. 17(a) shows that the development of the synthetic jet is confined within a narrow region close to the wall. Beneath the jet, striped vortices form due to the jet shear layer. As the velocity ratio increases, the shearing role of the synthetic jet is enhanced to produce a strong disturbance on the crossflow, aggravating the normal penetration and generating more complicated striped vortices in the wake flow zone behind the jet.

Figures 18 and 19 show the time-averaged jet center trajectories on the central plane and the area-integrated TKE distributions along the streamwise direction, respectively, at the three velocity ratios. These figures illustrate the effects of the velocity ratio on the penetration depth and the disturbing action of the synthetic jet in the crossflow. In general, with increasing velocity ratio, both the normal penetration and the range of influence of the synthetic jet in the crossflow are enhanced, resulting in greater area-integrated TKE.

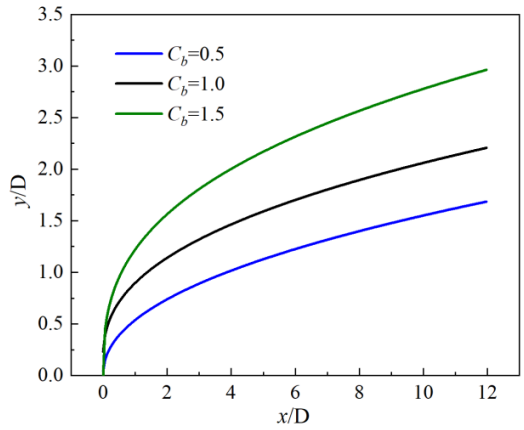

Fig. 18 Jet center trajectory for *AR* = 18 rectangular orifice

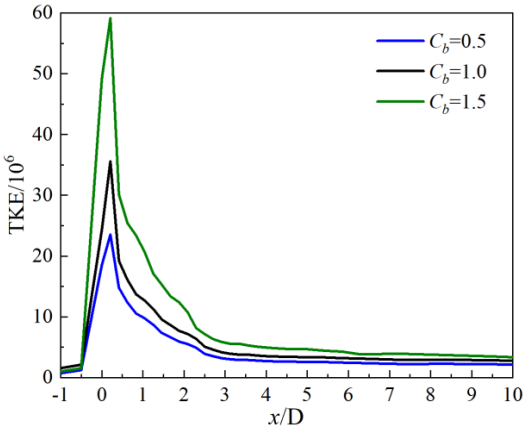

Fig. 19 Streamwise evolution of the area-integrated TKE for *AR* = 18 rectangular orifice

sing the wall shear stress (τ_0) in the absence of synthetic jet excitation as a reference, the dimensionless wall shear stress distributions (τ/τ_0, where τ is the time-averaged wall shear stress in the presence of synthetic jet) are presented in Fig. 20. This figure further illustrates the evolution of the coherent vortical structures. When compared with the pure crossflow, the presence of synthetic-jet excitation results in complicated vortical structures, which in turn lead to a significant increase in the wall shear stress, especially in the near-field region behind the orifice. In this near-field region, the shear stress exhibits fluctuations in the spanwise direction, which are attributed to the numerous unstable small-scale vortices in the near field. In the far-field region, the wall shear stress generally decreases in the streamwise direction. As the synthetic jet with a large velocity ratio has a strong normal penetration capacity, some detachment from and reattachment to the wall occurs, as shown in Fig. 19(c). In general, the flow field is mainly dominated by the sweeping of the CVP, which generates higher wall shear stress. With increasing velocity ratio, the extension ability of the striped zone with higher wall shear stress is significantly enhanced in the streamwise direction, having a stronger influence on the near-wall crossflow.

5. CONCLUSION

This study applied the LES framework to illustrate the coherent flow structures of synthetic jets in a crossflow. Round and rectangular orifices with the same area were considered. The influencing roles of the rectangular-orifice aspect ratio (*AR* = 6, 12, and 18) and the jet-to-crossflow velocity ratio (C_b = 0.5, 1.0, and 1.5) were analyzed in detail. The main conclusions can be summarized as follows:

(1) The FVR shed from the rectangular orifice lip behaves as a PV. The HV and FVR are followed by a trailing jet in the round-orifice situation, but this phenomenon is rarely identified in the case of a rectangular orifice. The PV splits into multiple small-scale vortex strings under the action of the crossflow. For the rectangular orifice with a large aspect ratio (*AR* = 18), VF structures form.

(2) Regardless of the orifice shape, the mutual interaction between the synthetic jet and the crossflow produces some identical or similar features. In general, at the same characteristic velocity, the round-orifice synthetic jet has a stronger normal penetration capacity in the crossflow, whereas the rectangular-orifice synthetic jet with a large *AR* develops closer to the wall.

3) The peak area-integrated TKE is greater in the round-orifice case than in the *AR* = 18 rectangular-orifice case. This is due to the strong normal penetration induced by the round orifice and the disturbance of the vortex

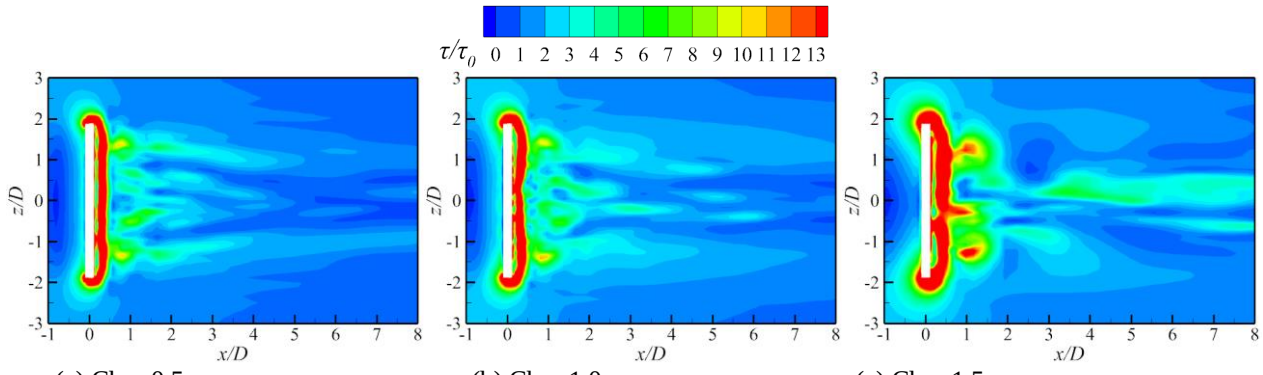

(a) Cb = 0.5 (b) Cb = 1.0 (c) Cb = 1.5

Fig. 20 Dimensionless wall shear stress distribution

cluster near the wall in the rectangular-orifice case. The rectangular-orifice synthetic jet with a large *AR* has a strong ability to extend downstream, and so the area-integrated TKE decays slowly along the streamwise direction.

(4) For the rectangular orifice with a large *AR*, the development of the synthetic jet is confined within a narrow space near the wall at a small jet-to-crossflow velocity ratio. An increase in the velocity ratio enhances both the normal penetration and the range of influence of the synthetic jet in the crossflow, resulting in greater area-integrated TKE and wall shear stress.

(5) Regarding the orifice shape, the round-orifice synthetic jet is more suitable for mixing enhancement, whereas the rectangular-orifice synthetic jet with a large *AR* is more suitable for boundary-layer flow control applications.

In this paper, the large eddy simulation of the rectangular orifice synthetic jet with a fixed frequency (1125Hz) is carried out. Later, the work will be extended to different frequencies to explore the influence of frequency on the rectangular orifice synthetic jet in the crossflow.

ACKNOWLEDGEMENTS

The authors are gratefully for the financial supports provided by Natural Science Fund of Jiangsu Province (BK20200448).

CONFLICT OF INTEREST

The authors declare that they have no competing interests.

AUTHORS CONTRIBUTION

Weimei Quan: Numerical investigation, data curation, formal analysis and writing original draft. **Wenjing Sun**: Methodology and formal analysis. **Jingzhou Zhang**: supervision and writing-review. **Xiaoming Tan**: supervision and writing-review.

REFERENCES

Arshad, A., Jabbal, M., & Yan, Y. (2020). Synthetic jet actuators for heat transfer enhancement – A critical review. *International Journal of Heat and Mass Transfer*, *146*, 118815. https://doi.org/10.1016/j.ijheatmasstransfer.2019.118815

Berk, T., Hutchins, N., Marusic, I., & Ganapathisubramani, B. (2018). Trajectory of a synthetic jet issuing into high-Reynolds-number turbulent boundary layers. *Journal of Fluid Mechanics*, *856*, 531–551. https://doi.org/10.1017/jfm.2018.734

Elimelech, Y., Vasile, J., & Amitay, M. (2011). Secondary flow structures due to interaction between a finite-span synthetic jet and a 3-D cross flow. *Physics of Fluids*, *23*(9), 094104. https://doi.org/10.1063/1.3632089

Eri, Q., Hong, L., Li, T., Wang, Q., & Wang, M. (2016). Numerical simulations of mixing enhancement in subsonic jet using high-momentum synthetic jets. *Journal of Propulsion and Power*, *32*(5), 1095–1103. https://doi.org/10.2514/1.B35801

Eroglu, A., & Breidenthal, R. E. (2001). Structure, penetration, and mixing of pulsed jets in crossflow. *AIAA Journal*, *39*(3), 417–423. https://doi.org/10.2514/2.1351

Feng, Y. Y., Song, Y. P., & Breidenthal, R. E. (2018). Model of the trajectory of an inclined jet in incompressible crossflow. *AIAA Journal*, *56*(2), 458–464. https://doi.org/10.2514/1.J056181

Garcillan, L., Zhong, S., Pokusevski, Z., & Wood, N. (2004, June 28). *A PIV study of synthetic jets with different orifice shape and orientation*. 2nd AIAA Flow Control Conference. 2nd AIAA Flow Control Conference, Portland, Oregon. https://doi.org/10.2514/6.2004-2213

Glezer, A., & Amitay, M. (2002). Synthetic jets. *Annual Review of Fluid Mechanics*, *34*(1), 503–529. https://doi.org/10.1146/annurev.fluid.34.090501.094913

Gordon, M., & Soria, J. (2002). PIV measurements of a zero-net-mass-flux jet in cross flow. *Experiments in Fluids*, *33*(6), 863–872. https://doi.org/10.1007/s00348-002-0518-4

Grenson, P., & Deniau, H. (2017). Large-Eddy simulation of an impinging heated jet for a small nozzle-to-plate distance and high Reynolds number. *International Journal of Heat and Fluid Flow*, *68*, 348–363. https://doi.org/10.1016/j.ijheatfluidflow.2017.09.014

Ho, H. H., Essel, E. E., & Sullivan, P. E. (2022). The interactions of a circular synthetic jet with a turbulent crossflow. *Physics of Fluids*, *34*(7), 075108. https://doi.org/10.1063/5.0099533

Hunt, J. C. R., Wray, A. A., & Moin, P. (1988). *Eddies, streams, and convergence zones in turbulence flows*. Center for Turbulence Research, Report CTR-S88 (Conference Paper CTR-S88; Center for Turbulence Research).

Jabbal, M., & Zhong, S. (2008). The near wall effect of synthetic jets in a boundary layer. *International Journal of Heat and Fluid Flow*, *29*(1), 119–130. https://doi.org/10.1016/j.ijheatfluidflow.2007.07.011

Jafarimoghaddam, A., Turkyilmazoglu, M., Roşca, A. V., & Pop, I. (2021). Complete theory of the elastic wall jet: A new flow geometry with revisited two-phase nanofluids. *European Journal of Mechanics - B/Fluids*, *86*, 25–36. https://doi.org/10.1016/j.euromechflu.2020.11.006

Jankee, G. K., & Ganapathisubramani, B. (2021). Interaction and vectoring of parallel rectangular twin jets in a turbulent boundary layer. *Physical Review*

Fluids, *6*(4), 044701. https://doi.org/10.1103/PhysRevFluids.6.044701

Karagozian, A. R. (2014). The jet in crossflow. *Physics of Fluids*, *26*(10), 101303. https://doi.org/10.1063/1.4895900

Li, B. B., Yao, Y., Gu, Y. S., & 1. (2016). Active control of 2D Backward facing step separated flow based on synthetic jet. *Acta Aeronautica et Astronautica Sinca*, *37*(6), 1753–1762. https://doi.org/10.7527/S1000-6893.2016.0014

Li, S., Luo, Z., Deng, X., Liu, Z., Gao, T., & Zhao, Z. (2022). Lift enhancement based on virtual aerodynamic shape using a dual synthetic jet actuator. *Chinese Journal of Aeronautics*, *35*(12), 117–129. https://doi.org/10.1016/j.cja.2022.06.005

Mahesh, K. (2013). The interaction of jets with crossflow. *Annual Review of Fluid Mechanics*, *45*(1), 379–407. https://doi.org/10.1146/annurev-fluid-120710-101115

Ostermann, F., Woszidlo, R., Nayeri, C. N., & Paschereit, C. O. (2020). Interaction between a crossflow and a spatially oscillating jet at various angles. *AIAA Journal*, *58*(6), 2450–2461. https://doi.org/10.2514/1.J058798

Purtell, L. P., & Klebanoff, P. S. (1981). Turbulent boundary layer at low Reynolds number. *Physics of Fluids*, *24*(5), 802–811. https://doi.org/10.1063/1.863452

Quan, W., Sun, W., Zhang, J., & Tan, X. (2023). Large-eddy simulations on interaction flow structures of pulsed jets in a crossflow. *Thermal Science and Engineering Progress*, *46*, 102221. https://doi.org/10.1016/j.tsep.2023.102221

Rathay, N., & Amitay, M. (2022). Interaction of synthetic jets with a massively separated three-dimensional flow field. *Physical Review Fluids*, *7*(3), 034702. https://doi.org/10.1103/PhysRevFluids.7.034702

Sahni, O., Wood, J., Jansen, K. E., & Amitay, M. (2011). Three-dimensional interactions between a finite-span synthetic jet and a crossflow. *Journal of Fluid Mechanics*, *671*, 254–287. https://doi.org/10.1017/S0022112010005604

Shoji, T., Besnard, A., Harris, E. W., M'Closkey, R. T., & Karagozian, A. R. (2019). Effects of axisymmetric square-wave excitation on transverse jet structure and mixing. *AIAA Journal*, *57*(5), 1862–1876. https://doi.org/10.2514/1.J057982

Smith, B. L., & Swift, G. W. (2003). A comparison between synthetic jets and continuous jets. *Experiments in Fluids*, *34*(4), 467–472. https://doi.org/10.1007/s00348-002-0577-6

Tan, X., Zhang, J., Yong, S., & Xie, G. (2015). An experimental investigation on comparison of synthetic and continuous jets impingement heat transfer. *International Journal of Heat and Mass Transfer*, *90*, 227–238. https://doi.org/10.1016/j.ijheatmasstransfer.2015.06.065

Turkyilmazoglu, M. (2019). Laminar slip wall jet of Glauert type and heat transfer. *International Journal of Heat and Mass Transfer*, *134*, 1153–1158. https://doi.org/10.1016/j.ijheatmasstransfer.2019.02.051

Van Buren, T., Beyar, M., Leong, C. M., & Amitay, M. (2016a). Three-dimensional interaction of a finite-span synthetic jet in a crossflow. *Physics of Fluids*, *28*(3), 037105. https://doi.org/10.1063/1.4943493

Van Buren, T., Leong, C. M., Whalen, E., & Amitay, M. (2016b). Impact of orifice orientation on a finite-span synthetic jet interaction with a crossflow. *Physics of Fluids*, *28*(3), 037106. https://doi.org/10.1063/1.4943520

Van Buren, T., Whalen, E., & Amitay, M. (2014). Vortex formation of a finite-span synthetic jet: Effect of rectangular orifice geometry. *Journal of Fluid Mechanics*, *745*, 180–207. https://doi.org/10.1017/jfm.2014.77

Wen, X., & Tang, H. (2014). On hairpin vortices induced by circular synthetic jets in laminar and turbulent boundary layers. *Computers & Fluids*, *95*, 1–18. https://doi.org/10.1016/j.compfluid.2014.02.002

Wu, D. K. L., & Leschziner, M. A. (2009). Large-Eddy simulations of circular synthetic jets in quiescent surroundings and in turbulent cross-flow. *International Journal of Heat and Fluid Flow*, *30*(3), 421–434. https://doi.org/10.1016/j.ijheatfluidflow.2009.01.007

Xia, X., & Mohseni, K. (2017). flow characterization and modeling of strong round synthetic jets in crossflow. *AIAA Journal*, *55*(2), 389–402. https://doi.org/10.2514/1.J054880

Xia, X., & Mohseni, K. (2018). Transitional region of a round synthetic jet. *Physical Review Fluids*, *3*(1), 011901. https://doi.org/10.1103/PhysRevFluids.3.011901

Zaman, K. B. M. Q., & Milanovic, I. (2012). Control of a jet-in-cross-flow by periodically oscillating tabsa). *Physics of Fluids*, *24*(5), 055107. https://doi.org/10.1063/1.4719150

Zhang, J., Xu, M., Pollard, A., & Mi, J. (2013). Effects of external intermittency and mean shear on the spectral inertial-range exponent in a turbulent square jet. *Physical Review E*, *87*(5), 053009. https://doi.org/10.1103/PhysRevE.87.053009

Zhang, J., Zhang, S., Wang, C., & Tan, X. (2020). Recent advances in film cooling enhancement: A review. *Chinese Journal of Aeronautics*, *33*(4), 1119–1136. https://doi.org/10.1016/j.cja.2019.12.023

Zhou, Y., Luo, Z. B., & Wang, L. (2022). Plasma syntheic jet actuator for flow control: Review. *Acta Aeronautica et Astronautica Sinca*, *43*(3), 025027. https://doi.org/10.7527/S1000-6893.2020.25027.